The Physicochemical and Electrochemical Characterization of Silver Nanoparticle-Incorporated Magnetite/Reduced Graphene Oxide

Azleen Rashidah Mohd Rosli[1], Nur Ayunie Kamaruzaman[1], Ainul Mardhiah Mansor[1], Noorashikin Md Saleh[2], Wan M. Khairul[1] and Farhanini Yusoff[1*]

[1]Faculty of Science and Marine Environment, Universiti Malaysia Terengganu, 21030 Kuala Nerus Terengganu, Malaysia

[2]Department of Chemical and Process Engineering, Faculty of Engineering and Built Environment Universiti Kebangsaan Malaysia, 43650 Bandar Baru Bangi, Selangor, Malaysia

*****Corresponding author (e-mail: farhanini@umt.edu.my)

In this paper, the physicochemical characterization and electrochemical behavior of a newly developed silver nanoparticle-incorporated magnetite/reduced graphene oxide (Ag-Fe_3O_4/rGO) are presented. The composites were synthesized by a simple approach of synthesis route combining the Hummer's method for synthesis of graphene oxide and the co-precipitation method for preparation of iron oxide. The physical characterization of the composites was studied using Fourier Transform Infrared (FTIR) spectroscopy, X-Ray Diffraction (XRD) analysis, Scanning Electron Microscopy (SEM), and Brunaeur-Emmet-Teller (BET) technique. Cyclic voltammetry (CV) technique and Electron Impedance Spectroscopy (EIS) were employed to study the electrochemical properties of Ag-Fe_3O_4/rGO. Results from the analyses signify a good electron transfer characteristic with high conductive and excellent capacitor nature of the modified electrocatalyst.

Keywords: Electrocatalyst; silver nanoparticles; magnetite; reduced graphene oxide

Received: January 2023; Accepted: March 2023

Chemical sensors can broadly detect various types of samples such as environmental samples or targeted gas analytes, while biosensors focus more on biological compounds, and these electrochemical sensors are preferable nowadays for detection of desired elements as they offer a low production cost and a more environmental-friendly system but with high selectivity and sensitivity [1-4]. Development of active sensing materials has attracted tremendous attention from researchers worldwide to improve electrochemical sensors for further use in large-scale industries or hospitals [5]. Moreover, nanotechnology's recent advancements have paved the way for a slew of novel materials with desirable features for a variety of electrochemical sensor applications. Magnetite (Fe_3O_4) nanoparticles have exceptional properties, including having substantial super-paramagnetic characteristics, biocompatibility, and being low/non-toxic [6-8]. Fe_3O_4 also has a large area of surface, which will help to improve electrical conduction of materials. However, because of the huge surface-to-volume ratio, Fe_3O_4 has high energies and is prone to agglomeration, which results in loss of magnetism and dispersibility, especially in large-scale syntheses. [9].

Due to the unique structural and electrical features, graphene-based metal oxide nanocomposites have lately piqued interest as a material for altering electrodes in order to address such serious concerns, whereas the removal of the functional oxygen groups in the reduction reaction of graphene oxide (GO) is able to enhance electrical conductivity, resulting in rGO which offers Fe_3O_4 a flexible substrate for the formation of hybrid nanocomposites with better characteristics [10,11]. The addition of magnetite to rGO enhances its capabilities, such as electrochemical stability, increased activity of electrocatalytic, and the ability of electron transfer, and prevents heavy aggregation. Ag nanoparticles are combined with Fe_3O_4 and rGO to boost the rate of electron transfer among nanocomposites and raise the sensitivity of modified electrodes due to their distinctive biocompatibility, stability of electrochemical, ease of finding, lower cost, and prolonged electrocatalytic performance [12-14]. The beneficial properties of each parent component are demonstrated by nanocomposites of graphene, silver, and magnetic nanoparticles, providing a material with remarkable physicochemical properties and improved catalytic efficiency that has been extensively researched in the field of catalysis and sensor platforms.

Numerous studies have been conducted for the synthesis of graphene-based composites, such as the binary of metal-graphene or polymer-graphene. To the best of our knowledge, there is still a lack of studies into the development of graphene-based ternary nanocomposites of metal-graphene hybrid, as well as for their properties. In this study, ternary nanocomposites

of silver nanoparticles incorporated with magnetite/reduced graphene oxide (Ag-Fe_3O_4/rGO) were developed by a simple one-pot technique. The nanocomposites were subjected to physicochemical and electrochemical analyses to determine their properties. The results obtained from these analyses could offer insights into the development of novel catalysts for various electrochemical applications.

EXPERIMENTAL

Materials and Apparatus

Natural graphite powder, iron(II) chloride tetrahydrate/ferrous chloride ($FeCl_2.4H_2O$, 99.5%), iron(III) chloride hexahydrate/ferric chloride ($FeCl_3.6H_2O$, 99.5%), and sodium borohydride ($NaBH_4$) were acquired from R&M Chemicals (Kuala Lumpur, Malaysia). Hydrochloric acid (HCl, 5%), silver nitrate ($AgNO_3$), alumina powder (AlO_3), potassium ferrocyanide ($K_4[Fe(CN)_4]$, 99.9%), and potassium chloride (KCl) were acquired from Merck (Darmstadt, Germany).

Instrumentation

The physical features of the composites were determined using Fourier Transform Infrared Spectroscopy (FTIR, IR-Tracer 100, Shimadzu spectrophotometer), spectral range of 3500 cm^{-1} - 500 cm^{-1}; Scanning Electron Microscopy (SEM, JEOL JSM 6360LA), operating voltage of 5 kV; and X-Ray Diffractometer (XRD, Rigaku MiniFlex II), 2θ values of 3° to 90°. Brunaur-Emmet-Teller Analysis (BET, ASAP 2020 Micrometrics) was also utilized to determine the physical features of the composites. A potentiostat/galvanostat (Autolab PGSTAT302N with NOVA 1.10 software), using the three-electrode setup was used to determine the electrochemical characterization of Ag-Fe_3O_4/rGO. The three-electrode setup: glassy carbon electrodes (BASi, 3.0 mm diameter) modified with the composites as the working electrode, an Ag/AgCl (3.0 M KCl) reference electrode, and a platinum wire as the auxiliary electrode.

Synthesis of Ag-Fe_3O_4/rGO

The Hummer's technique yielded 50 mg of GO flakes, which was dispersed in 130 mL of distilled water and labelled as solution I [15]. A molar ratio of 2:1 of ferric chloride and ferrous chloride was added into 20 mL of distilled water and labelled as solution II. Solution II was then slowly added to solution I at room temperature. Then, 2 or 3 pieces of sodium hydroxide pellets were added to the mixture to attain the pH in the range of 9-10. Sodium hydroxide functions in aiding the precipitation of Fe^{2+}. The mixture was then heated to 80°C and constantly stirred until a black precipitate was formed [16]. The mixture was then centrifuged to separate Fe_3O_4/GO from the solvent. After separation, Fe_3O_4/GO was rinsed with deionized water. To introduce the Ag nanoparticles to Fe_3O_4/GO, 79 mg of silver nitrate was added to Fe_3O_4/GO and the mixture was stirred for 30 minutes. A reduction agent, sodium borohydride, was used in this study to reduce GO to rGO chemically, and the mixture was stirred continuously for two hours at 80°C. The homogeneous mixture was then filtered using a 3:1 molar ratio of HCl: distilled water, and the residue was dried overnight at 60°C in the oven. The synthesis is shown in Figure 1.

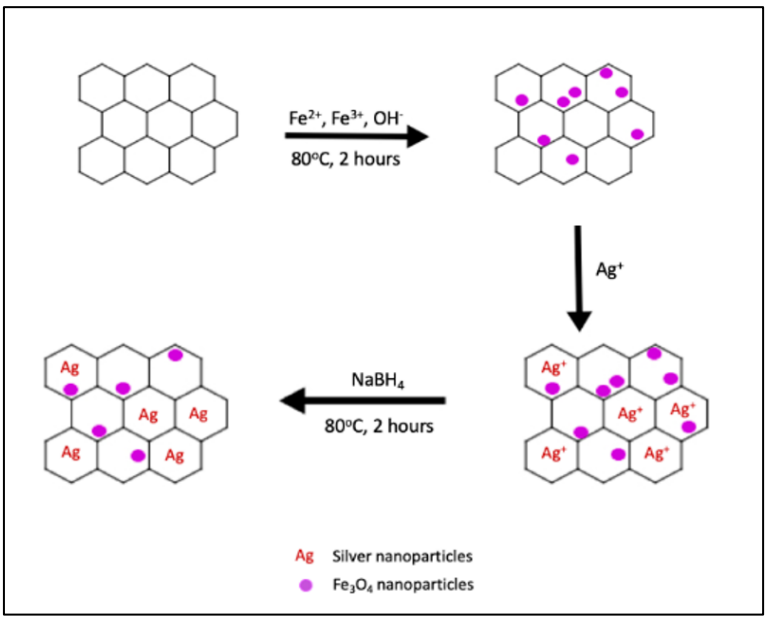

Figure 1. Synthesis of Ag-Fe_3O_4/rGO.

Fabrication of Modified GCEs

A small amount of aluminium oxide (alumina powder) was added with a few drops of deionized water, while glassy carbon electrodes were waxed before being rinsed with aluminium oxide slurry. To obtain a homogenous Ag-Fe_3O_4/rGO mixture, 10 mg of Ag- Fe_3O_4/rGO powder was diffused in 10 mL of deionized water and sonicated for 10 minutes. At least 7 µL of Ag-Fe_3O_4/rGO mixture was cast onto the GCEs, and the modified GCEs were left to dry at room temperature.

RESULTS AND DISCUSSION

Fourier Transform Infrared Analysis (FTIR)

FTIR spectroscopy was employed to assess the functionalities, as well as the bonding interactions and vibrational modes of each synthesized composite. The FTIR spectra of the composites are shown in Figure 2. From Figure 2(a), the GO spectrum showed a large stretching peak of hydroxyl group O-H at 3246 cm^{-1}, due to the adsorption of water molecules at the graphene sheets throughout the synthesis process [17]. The carboxylic group C=O at the edge of the graphene sheets was assigned an absorption band reported at 1739 cm^{-1}, while the intensity of the intense absorption peak at 1620 cm^{-1} correlated to the stretching vibration of the unoxidized graphitic domain of C = C bond [18]. The hydroxyl group's O-H bending vibration and deformation occurred at 1359 cm^{-1}, while the 1219 cm^{-1} and 1041 cm^{-1} absorption peaks belonged to the stretching of C-O epoxy and C-O alkoxy, respectively.

Meanwhile, from Figure 2(b), the Fe_3O_4/rGO spectrum showed an absorption peak at 3377 cm^{-1} of broad O-H stretching, due to the abundant use of water during the wet synthesis method of Fe_3O/rGO. The C=O stretching vibration mode at 1739 cm^{-1}, deformation vibration of C-H bond at 1365 cm^{-1}, and C-O epoxy stretching vibration at 1217 cm^{-1} appeared in the Fe_3O_4/rGO spectrum due to the addition of Fe_3O_4 into the rGO sheets [19]. Meanwhile, the 530 cm^{-1} absorption peak was attributed to Fe-O, and increase in the intensity of the vibration peak represented the iron load in the Fe_3O_4/rGO composite.

The introduction of silver into the Fe_3O_4/rGO materials did not alter the Fe_3O_4/rGO spectrum, but the Ag-Fe_3O_4/rGO spectrum (Figure 2(c)) was found to be more intense in peaks. The presence of a strong alcohol group O-H stretch absorption peak at 3014 cm^{-1} was found to be different from the broad Fe_3O_4/rGO O-H stretch (3377 cm^{-1}). The Ag-Fe_3O_4/rGO spectrum presented more intensive peaks of C=O stretching at 1739 cm^{-1}, C-H deformation and bending vibration at 1365 cm^{-1}, and C-O epoxy stretching at 1217 cm^{-1}. Meanwhile, a new absorption peak at 900 cm^{-1} indicated a C=C bending from a monosubstituted alkene and a Fe-O stretch peak at 528 cm^{-1} was more intense compared to Fe_3O_4/rGO. An absorption peak at 447 cm^{-1} indicating Ag metal was present in the hybrid materials [20,21].

X-Ray Diffraction Analysis (XRD)

The structural phase of crystalline materials was investigated using XRD analysis. The XRD diffraction spectrum of GO revealed an intense 2θ peak at 10.10°, which corresponds to the (0 0 1) crystal plane, as illustrated in Figure 3(a). The diffraction peak demonstrated that the graphite layer had expanded because of the addition of an oxygen functional group to the graphene layers [22].

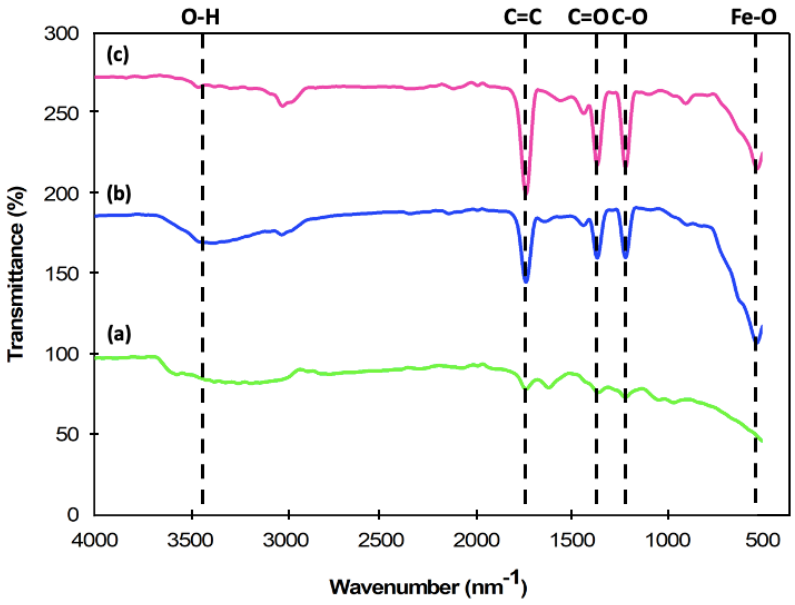

Figure 2. FTIR spectra of (a) GO, (b) Fe_3O_4/rGO, and (c) Ag-Fe_3O_4/rGO.

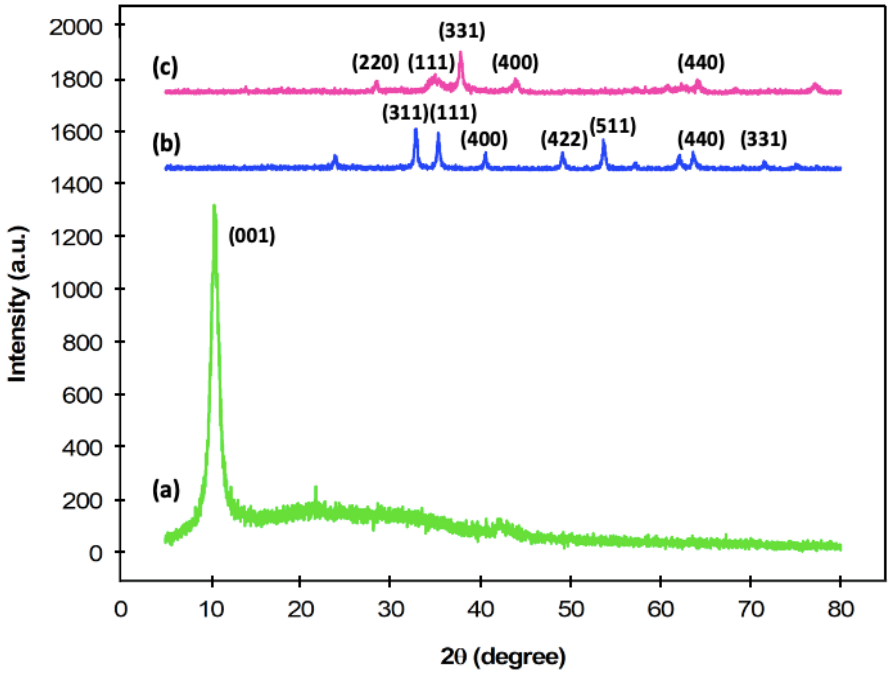

Figure 3. XRD diffraction spectra of (a) GO, (b) Fe_3O_4/rGO, and (c) Ag-Fe_3O_4/rGO.

The Fe_3O_4/rGO diffraction spectrum (Figure 3(b)) constituted a series of 2θ diffraction peaks of 35.5°, 43.3°, 53.7°, 57.3°, 62.8°, and 74.09°, which correspond to crystal planes of (3 1 1), (4 0 0), (4 2 2), (5 1 1), and (4 0 0) (JCPDS card: 19-0629), respectively [23]. In the meantime, Figure 3(c) displays the 2θ diffraction peaks of Ag- Fe_3O_4/rGO with intense peaks of 28.5°, 34.7°, 43.9°, and 62.4°, which are well indicated to (2 2 0), (3 1), (4 0 0), and (4 4 0) spinel Fe_3O_4 lattice planes, suggesting the presence of Fe_3O_4 on the rGO substrate (JCPDS card: 04-0783) [24]. The XRD diffraction spectrum of crystalline silver showed an intense diffraction peak at 2θ=37.8°, which corresponds a lattice plane of (1 1 1). Interestingly, the graphitic peak (0 0 1) of GO of Ag-Fe_3O_4/rGO was absent due to the deposition of attached Fe_3O_4 and Ag to rGO, prohibiting van der Waals interactions from forming and the stacking interactions between the rGO sheets [25].

From the XRD data obtained, there were several parameters that could be calculated, such as the interplanar spacing, *d* between the graphitic layer and the out-of-plane crystallite size, D of the graphitic layer. The d-spacing value for each individual material was calculated using the Bragg's law equation in Equation 1 below.

$$d = \frac{\lambda}{2\sin\theta} \qquad \text{(Equation 1)}$$

Where λ is the X-ray wavelength of the Cu-K alpha wavelength, which is 0.154 nm, and θ is the half of corresponding diffraction angle. Meanwhile, for the crystallite size, D, the calculated value is given by the Debye-Scherer equation in Equation 2 below, where β is the diffraction peak of whole width in radians at half maximum height. The FWHM value was generated by the software PDXL for the XRD analysis used. λ is the X-ray wavelength, which in this characterization study we used the Cu-K alpha wavelength of 0.154 nm and θ is the half of 2θ obtained from the analysis.

$$D = \frac{K\lambda}{\beta\cos\theta} \qquad \text{(Equation 2)}$$

Table 1 presents the resultant *d*-spacing and crystallite size obtained, which indicate Ag- Fe_3O_4/ rGO gave the highest crystallite size of 26.76 nm, as compared to Fe_3O_4/rGO and GO crystallite size values of 10.96 nm and 6.64 nm, respectively. A similar trend was observed for FWHM. This might be due to the incorporation of iron oxide and silver respectively in the nanocomposites. Incorporation of these metals into nanocomposites could cause changes in their crystalline structures, resulting in increases in crystallite size, *d*-spacing, and FWHM observed in the analysis. These changes could occur due to strain, disorder, defects, or nucleation/growth of larger crystallites induced by the presence of the metals.

Table 1. Parameters of catalyst obtained from XRD analysis.

Composites	2θ (degree)	FWHM (degree)	*d* (nm)	D (nm)
GO	10.09	1.25	0.88	6.64
Fe_3O_4/rGO	62.81	0.89	0.15	10.96
Ag-Fe_3O_4/rGO	28.48	0.32	0.31	26.76

Scanning Electron Microscopy (SEM)

The surface structure of the generated composites was investigated using SEM analysis. Figure 4 presents the surface structures of the composites GO, Fe_3O_4/ rGO, and Ag- Fe_3O_4/rGO. The GO surface micrograph (Figure 4(a)) revealed a smooth surface with a distinctive layered, similar to paper-like appearance. Due to the exfoliation of graphite, the wrinkle surface structure may be clarified when the carboxyl, hydroxyl, and epoxy groups were introduced onto the edge of the graphene sheets during the GO synthesis process [26].

Consequently, the formation of Fe_3O_4/rGO was verified, as shown in Figure 4(b), by the SEM micrograph demonstrating that the sphere-shaped structure of Fe_3O_4 was attached to the exfoliated rGO layer, suggesting that rGO was effectively coated with the Fe_3O_4 composites [27]. The average particle size of Fe_3O_4 in the Fe_3O_4/rGO composites was substantially lower than that of Fe_3O_4 alone, showing that rGO had reduced Fe_3O_4 crystal formation to some extent. Meanwhile, the SEM micrograph of Ag-Fe_3O_4/rGO (Figure 4(c)) showed a similar pattern of the sphere-shaped structure of Fe_3O_4 but with increasing abundance of smaller structures, which indicated the smaller size of Ag nanoparticles attached to the rGO layer [28].

Energy Dispersive X-Ray Spectroscopy (EDS) study was also carried out to better understand the element distribution in each synthesized composite. Table 2 demonstrates the elemental percentage of each element. The calculated mass percentage of each element in GO was O (22.27%) and C (77.73%), demonstrating that GO was successfully synthesized with no impurities using the modified Hummer's method [29].

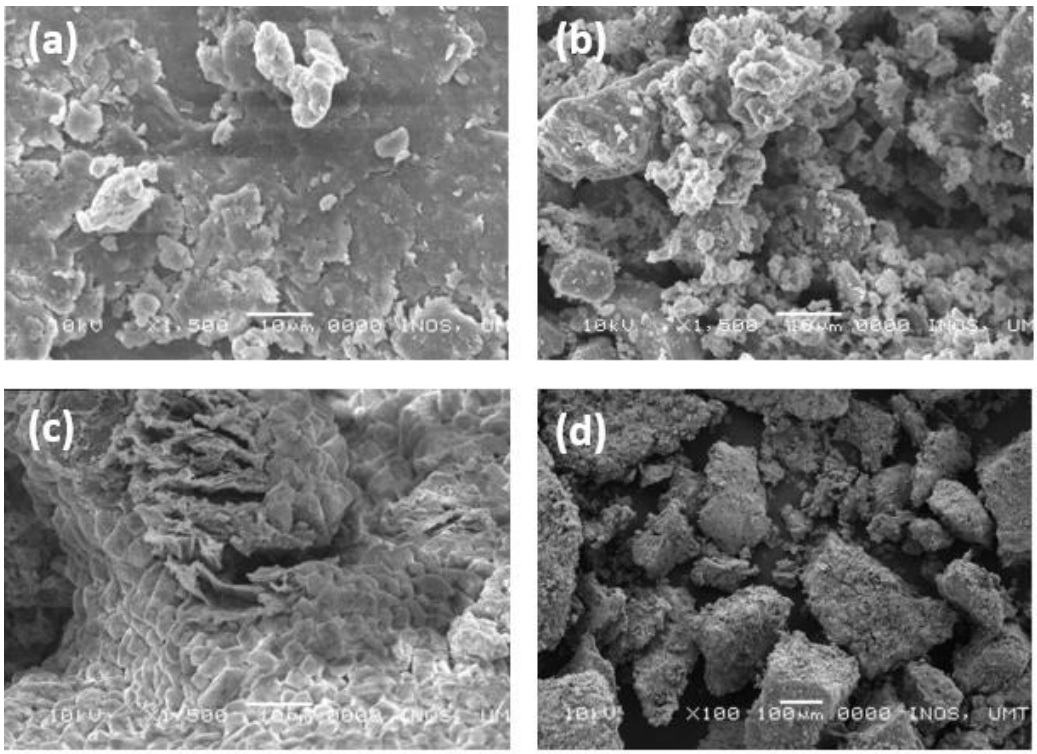

Figure 4. SEM micrographs of (a) GO, (b) Fe_3O_4, (c) Fe_3O_4/rGO, and (d) Ag-Fe_3O_4/rGO at operational voltage 10 kV and magnification of x1500.

Table 2. Elemental percentages obtained from EDS analysis.

Composites	Element	Mass %	Atomic %
GO	O	22.27	-
	C K	77.73	100
Fe_3O_4/rGO	O	10.00	-
	C K	65.23	66.53
	Fe K	24.47	33.47
Ag-Fe_3O_4/rGO	O	14.79	-
	C K	49.24	64.89
	Fe K	18.88	23.54
	Ag L	11.73	10.57

For Fe_3O_4/rGO, the measured mass percentages for elements O, C, and Fe were 10.00 percent, 65.23 percent, and 24.77 percent, respectively, indicating that the incorporation of Fe_3O_4 on rGO had lowered the composite's mass percentages of carbon and oxygen significantly. In the Ag- Fe_3O_4/rGO composite, the mass percentages for elements O, C, Fe, and Ag were determined to be 14.79 percent, 49.24 percent, 18.88 percent, and 11.73 percent, respectively. Compared to the Fe_3O_4/rGO EDS mass percentage and the mass ratio of Ag: Fe_3O_4:rGO (1:2:7) based on the feed ratio, the integrated silver nanoparticles on Fe_3O_4 and rGO had decreased the mass percentages of carbon, oxygen, and iron slightly.

Brunauer-Emmet-Teller Analysis (BET)

The BET approach calculates total precise region from exterior and pore area measurements, which is valuable for analyzing surface porosity effects, pore properties, and particle size, as described in Table 3. The surface area, pore volume, and pore size of GO increased rapidly, reaching 408.57 m^2/g for the BET surface area, 545.79 m^2/g for the Langmuir surface area, 1.98 cm^3/g for pore volume, and 23.27 nm for pore size. This reveals that the total surface area of the composite has been increased by the addition of oxygen functionality to GO. According to Chen et al. (2020), the theoretical value of the BET surface area gives a value of 400 m^2/g, which is very similar to the experimental value obtained. The increase in surface area obtained could be owing to partial graphite oxidation, and the small aggregation of graphene sheets during oxidation could potentially affect the porosity properties of GO [30].

The sediment of silver on the Fe_3O_4/rGO composite, in particular, reduced the surface area characteristics of Ag- Fe_3O_4/rGO, as well as the volume and size of pores. Due to its low surface areas of 73.64 m^2/g (BET surface area) and 102.48 m^2/g (Langmuir surface area), Ag Fe_3O_4/rGO is expected to generate a high diffusion rate and an increase of charge transfer between the redox probe and the electrode surface [31].

Electrochemical Behavior of Modified Electrodes

The performance of the bare and modified electrodes towards the electrocatalytic behavior in standard supporting electrolytes of KCl and $K_4[Fe(CN)_6]$ was investigated utilizing a cyclic voltammetry (CV) technique employing the Potentiostat/Galvanostat (PGSTAT). The redox probe $K_4[Fe(CN)_6]$ has been widely used as a tracer to measure the rate of electron transfer of modified electrodes due to its high sensitivity and near quasi-reversibility to carbon-based electrodes. Figure 5 shows cyclic voltammogram of individual modified electrode and unmodified bare GCE in selected parameters.

Table 3. Parameters obtained from BET analysis.

Composites	BET surface area (m^2/g)	Langmuir surface area (m^2/g)	Pore volume (cm^3/g)	Pore size (nm)
GO	408.57	545.79	1.98	23.27
Ag-Fe_3O_4/rGO	73.64	102.48	0.15	7.97

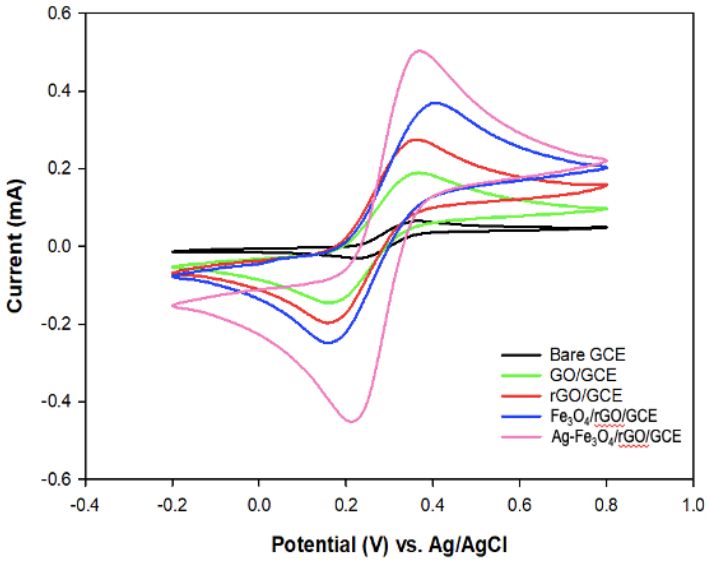

Figure 5. Cyclic voltammograms of composite-modified electrodes at rate of scanning of 100 mV/s (Electrolyte: 5.0 mM of $K_4[Fe(CN)_6]$ in 1.0 M KCl solution).

Both the unmodified and modified GCEs exhibited a well-defined relatively reversible redox peak, as indicated by the voltammogram, implying that the electron transfer between the $[Fe(CN)_6]^{-3/-4}$ redox probe and the electrode surface was stable. The increasing peak current followed the order of bare GCE < GO/GCE < rGO/GCE < Fe_3O_4/rGO/GCE < Ag- Fe_3O_4/rGO/GCE.

Obviously, the Ag-Fe_3O_4/rGO/GCE redox peak current increased significantly 3-fold higher compared with the bare GCE. This enhanced electrochemical behavior may be linked to Ag- Fe_3O_4/rGO's excellent electrical conductivity on the GCE surface which speeds up the rate of electron transfer of the modified electrode at the electrode/electrolyte interface [32]. AgNPs and Fe_3O_4 play a major role in raising the electroactive surface, which enhances the electro-chemically active surface and accelerates the relatively rapid transfer rate of electrons at modified electrode surfaces [33].

Electron Impedance Spectroscopy (EIS)

Electron Impedance Spectroscopy (EIS) was used to analyze the improvement of the charge transfer property on the surface of the electrodes. The information obtained was then used to study the rate of electron transfer, the impedance of electrons, the resistance to the charge transfers, and the capacity of the double layer of bare GCE, GO/GCE, rGO/GCE, Fe_3O_4/rGO/GCE, and Ag- Fe_3O_4/rGO/GCE.

Figure 6 shows the Nyquist plots of the bare and modified electrodes in the electroactive marker ions $[Fe(CN)_6]^{-3/-4}$ in the frequency range of 1 Hz to 10,000 Hz. Generally, the resistance of solution (R_s), the resistance of charge transfer (R_{ct}), and Warburg impedance (Z_w) are usually included in a Nyquist plot. The resistance of the electrolyte solution is represented by R_s at the high frequency intersection with the Z' axis, whereas the resistance of the electrode/electrolyte interface is represented by R_{ct} in the high frequency area by the Nyquist plot's semicircle shape. At the low frequency intersection, a linear plot of the Nyquist represents the diffusion-controlled process between the surface of electrode and the electrolyte [37].

The results showed that the bare GCE has a visible semicircle, indicating a higher impedance than the other modified GCEs of GO, rGO, Fe_3O_4/rGO, and Ag- Fe_3O_4/rGO that have no semicircle, which shows a low resistive characteristic. These low resistance features are thought to aid the modified electrodes' electron transfer rate [38].

Meanwhile, for all the modified electrodes, a vertical straight line demonstrating diffusion and capacitive behavior could be observed at a low frequency area. The Ag- Fe_3O_4/rGO/GCE showed the largest slope of the straight line of nearly 90° compared to the unmodified and other modified GCEs, implying to Warburg impedance response [39]. Compared to another modified electrode, the compound- modified GCE had the best capacitive properties due to the fast diffusion rate and kinetic transport of electro-active marker ions in the electrolyte governed by the Ag- Fe_3O_4/rGO/GCE.

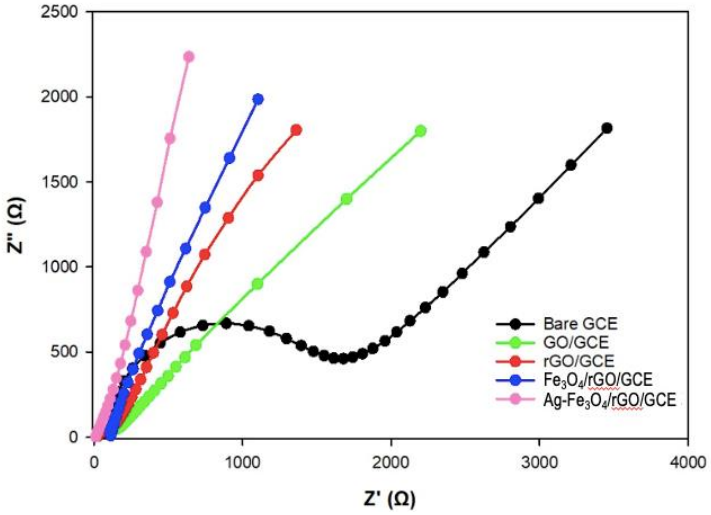

Figure 6. Nyquist plots of bare and composite-modified electrodes in 5.0 mM $K_4[Fe(CN)_6]$ and 1.0 M KCl supporting electrolyte.

Figure 7 depicts the suggested Randles equivalent circuit for characterizing the impedance behavior of the different electrodes used from the Nyquist diagram. For the redesigned electrode, the Rs[CPE($R_{ct}Z_w$)C] Randles circuit was replaced with the Rs[CPE ($R_{ct}Z_w$)]C equivalent circuit model. In the meantime, Table 4 lists the values of each changed GCE's fitting parameters.

The R_s value of the bare GCE was the highest in interpretation of the results listed in Table 4, while the R_s value of the Ag-Fe_3O_4/rGO/GCE was found to be relatively low among the modified electrodes. This implies that the bare GCE displayed a large resistance activity in the electrolyte interface, and the modified electrode possessed a low resistive behavior in the solution. Implementing Fe_3O_4 and Ag into the composite also significantly improved electrode resistive activity within the electrolyte interface. The charge transfer resistance between the unmodified and modified electrodes followed a similar pattern, with the bare GCE having the greatest R_{ct} value and the Ag-Fe_3O_4/rGO/GCE having the lowest R_{ct} value when compared to the other modified GCEs. The patterns and values showed the Ag-Fe_3O_4/rGO/GCE possessed low resistive features towards the electrolyte resistance and charge transfer resistance [32,36].

Equation 3 below was used to calculate the visible electron transfer rate constant (K_{app}) value for each changed electrode, where R is the gas constant, T is the ambient temperature in Kelvin, n is the number of moles of electrons transferred in the redox reaction, A is the diameter area of the electrode used, F is the Faraday constant, and C is the concentration of redox probe in mol/cm^3 [37].

$$K_{app} = \frac{RT}{n^2 F^2 A R_{ct} C} \qquad \text{(Equation 3)}$$

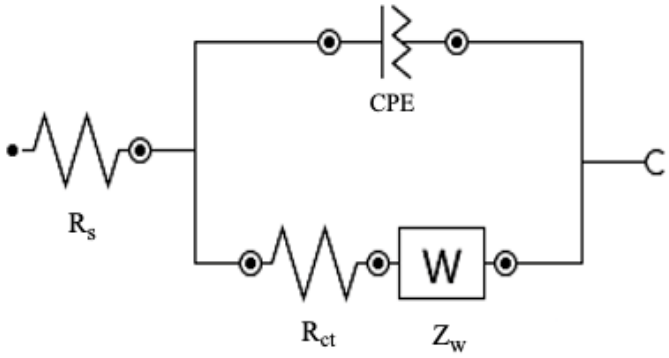

Figure 7. The altered Randles circuit model that consists of the resistance of solution (R_s), the resistance of charge transfer (R_{ct}), constant phase element (CPE), Warburg diffusion element (Z_w), and capacitance (C).

Table 4. Parameters of EIS fittings of unmodified and modified electrodes.

Modified Electrode	$R_s/\Omega m^2$	$R_{ct}/\Omega m^2$	K_{app}/cms^{-1}
Bare GCE	83.0	540.0	$3.23x10^{-4}$
GO/GCE	72.2	491.1	$3.55x10^{-4}$
rGO/GCE	61.0	53.0	$3.29x10^{-3}$
Fe_3O_4/rGO/GCE	46.3	13.8	$1.26x10^{-2}$
Ag-Fe_3O_4/rGO/GCE	43.2	7.9	$2.20x10^{-2}$

The high conductive graphene helped to improve the transfer of electron on the surface of an electrode, while the rich oxygen function in rGO enhanceed the conductivity property of a composite and therefore boosted the rate of electron transfer [40]. The introduction of high area of surface of Fe_3O_4 and AgNPS also aided the electron transfer rate of the composites. Thus, the highest K_{app} value for the Ag-Fe_3O_4/rGO/GCE confirms that the modified electrode has an effective electron transfer rate compared to the unmodified and other modified electrodes.

CONCLUSION

In summary, a Ag-Fe_3O_4/rGO nanocomposite has been successfully synthesized using a simple one-pot method. The XRD data revealed that the Ag-Fe_3O_4/rGO composite has the highest crystallite size (26.76 nm) compared to Fe_3O_4/rGO (10.96 nm) and GO (6.64 nm). The BET analysis showed that the Ag-Fe_3O_4/rGO composite has the lowest surface area (73.64 m^2/g), which is indicative of a high diffusion rate and an increase in charge transfer between the redox probe and the electrode surface. The electrochemical properties of the Ag-Fe_3O_4/rGO composite showed the largest slope of the straight line of nearly 90°, implying a Warburg impedance response, and a high K_{app} value, indicating an effective electron transfer rate. These properties make the Ag-Fe_3O_4/rGO composite a promising catalytic electrocatalyst for various electrochemical applications. Overall, the physicochemical and electrochemical characterization data of the Ag-Fe_3O_4/rGO composite demonstrate its superior catalytic activity against the $K_4[Fe(CN)_6]$ redox reaction compared to other modified GO, rGO, and Fe_3O_4/rGO electrodes, making it a potential candidate for future electrochemical applications.

ACKNOWLEDGEMENT

The authors acknowledge the funding of the Ministry of Education through the Fundamental Research Grant Scheme (FRGS) FRGS/1/2021/STG04/UMT/02/1 and the Central Laboratory UMT research facilities.

REFERENCES

1. Albar, M. M. J., Jamion, N. 'Ain, Baharin, S. N. A., Raoov, M. & Sambasevam, K. P. (2020) Preparation of novel commercial polyaniline composites for ammonia detection. In *Solid State Phenomena: Trans Tech Publications Ltd.*, **301** (SSP), 124–131.

2. Mohd Norsham, I. N., Baharin, S. N. A., Raoov, M., Shahabuddin, S., Jakmunee, J. & Sambasevam, K. P. (2020) Optimization of waste quail eggshells as biocomposites for polyaniline in ammonia gas detection. *Polymer Engineering and Science*, **60(12)**, 3170–3182.

3. Derbali, M., Othmani, A., Kouass, S., Touati, F. and Dhaouadi, H. (2020) $BiVO_4/TiO_2$ nano-composite: Electrochemical sensor for hydrogen peroxide. *Materials Research Bulletin*, **125**, 110771.

4. Wang, S., Guo, P., Ma, G., Wei, J., Wang, Z., Cui, L., Sun, L. and Wang, A. (2020) Three-dimensional hierarchical mesoporous carbon for regenerative electrochemical dopamine sensor. *Electrochimica Acta*, **360**, 137016.

5. Lahcen, A. A., Rauf, S., Beduk, T., Durmus, C., Aljedaibi, A., Timur, S., Alshareed, H. N., Amine, A., Wolfbeis, O. S., and Salama, K. N. (2020) Electrochemical sensor and biosensor using laser-derived graphene: A comprehensive review. *Biosensor Bioelectronic*, **168**, 112565.

6. Hou, X., Xu, H., Zhen, T. and Wu, W. (2020) Recent developments in three-dimensional graphene-based electrochemical sensors for food analysis. *Trends in Food Science Technology*, **105**, 76–92.

7. Si, Y. and Lee, H. J. (2020) Carbon nanomaterials and metallic nanoparticles-incorporated electrochemical sensors for small metabolites: Detection methodologies and applications. *Current Opinion in Electrochemistry*, **22**, 234–243.

8. Cai, L., Hou, B., Shang, Y., Xu, L., Zhou, B., Jiang, X. and Jiang, X. (2019) Synthesis of Fe_3O_4/graphene oxide/pristine graphene ternary composite and fabrication electrochemical sensor to detect dopamine and hydrogen peroxide. *Chemical Physics Letter*, **736**, 136797–136802.

9. Fayemi, O. E., Adekunle, A. S., Kumara-Swamy, B. E. and Ebenso, E. E. (2018) Electrochemical sensor for the detection of dopamine in real sample using polyaniline/NiO, ZnO and Fe_3O_4 nanocomposites on glassy carbon electrode. *Journal of Electroanalytical Chemistry*, **818**, 236–249.

10. Ratnam, K. V., Manjunatha, H., Janardan, S., Babu-Naidu, K. C. and Ramesh, S. (2020) Nonenzymatic electrochemical sensor based on metal oxide, MO (M= Cu, Ni, Zn, and Fe) nanomaterials for neurotransmitters: An abridged review. *Sensors International*, **1**, 100047–100052.

11. Sohouli, E., Khosrowshahi, E. M., Radi, P., Naghian, E., Rahimi-Nasrabadi, M. and Ahmadi, F. (2020) Electrochemical sensor based on modified methylcellulose by graphene oxide and Fe_3O_4 nanoparticles: Application in the analysis of uric acid content in urine. *Journal of Electroanalytical Chemistry*, **877**, 114503.

12. Zhang, H. and Liu, S. (2020) Electrochemical sensors based on nitrogen-doped reduced graphene oxide for the simultaneous detection of ascorbic acid, dopamine and uric acid. *Journal of Alloys and Compounds*, **842**, 155873.

13. He, W., Liu, R., Zhou, P., Liu, Q. and Cui, T. (2020) Flexible micro-sensors with self-assembled graphene on a polyolefin substrate for dopamine detection. *Biosensor Bioelectronic*, **167**, 112473

14. Ma, S., Yang, Q., Zhang, W., Xia, G., Wang, M., Cheng, L., Zhou, X., Zhao, M., Ji, J. and Yue, Z. (2020) Silver nanoclusters and carbon dots based light-addressable sensors for multichannel detection of dopamine and glutathione and its application in probing of Parkinson's disease. *Talanta*, **219**, 121290.

15. Hyder, M., Reddy, G. R. K., Naveen, B. and Kumar, P. S. (2020) Copper-silver bimetallic nanoelectrocatalyst on pencil graphite substrate for highly sensitive amperometric dopamine sensor. *Chemical Physics Letter*, **740**, 137086.

16. Shen, J., Sun, C. and Wu, X. (2017) Silver nanoprisms-based Tb(III) fluorescence sensor for highly selective detection of dopamine. *Talanta*, **165**, 369–376.

17. Alkhouzaam, A., Qiblawey, H., Khraisheh, M., Atieh, M. and Al-Ghouti, M. (2020) Synthesis of graphene oxides particle of high oxidation degree using a modified Hummers method. *Ceramics International*, **46(15)**, 23997–24007.

18. Adyani, S. H., and Soleimani, E. (2018) Green synthesis of Ag/Fe_3O_4/RGO nanocomposites by Punica Granatum peel extract: Catalytic activity for reduction of organic pollutants. *International Journal of Hydrogen Energy*, **44(5)**, 2711–2730.

19. Kalaiarasi, S., Kavitha, M., Karpagavinayagam, P., Vedhi, C. and Muthuchudarkodi, R. R. (2020) Tungsten oxide decorated graphene oxide nanocomposite: Chemical synthesis, characterization and application in super capacitors. *Materials Today: Proceedings*, **1**.

20. Kakaei, K. and Rahnavardi, M. (2020) Synthesis of nitrogen-doped reduced graphene oxide and its decoration with high efficiency palladium nanoparticles for direct ethanol fuel cell. *Renewable Energy*, **163**, 1277–1286.

21. Harnchana, V., Chaiyachad, S., Pimanpang, S., Saiyasombat, C., Srepusharawoot, P. and Amornkitbamrung, V. (2019) Hierarchial Fe_3O_4-reduced graphene oxide nanocomposite grown on NaCl crystals for triiodide reduction in dye-sensitized solar cells. *Scientific Report*, **9(1)**, 1494.

22. Thu, T. V., Ko, P. J., Nguyen, T. V., Vinh, N. T., Khai, D. M. and Lu, L. T. (2017) Green synthesis of reduced graphene oxide/Fe_3O_4/Ag ternary nanohybrid and its application as magnetically recoverable catalyst in the reduction of 4-nitrophenol. *Applied Organomettalic Chemistry*, **31(11)**, 1.

23. Tan, W. K., Asami, K., Maegawa, K., Kumar, R., Kawamura, G., Muto, H. and Matsuda, A. (2020) Fe_3O_4-embedded rGO composites as anode for rechargeable FeO_x-air batteries. *Materials Today Communication*, **25**, 101540.

24. Guan, X. H., Li, M., Zhang, H. Z., Yang, L. and Wang, G. S. (2018) Template-assisted synthesis of $NiCoO_2$ nanocages/reduced graphene oxide composites as high-performance electrodes for supercapacitors. *RSC Advance*, **8**, 16902–16909.

25. Zhu, A., Shi, P., Sun, S. and Rui, M. (2019) Construction of rGO/ Fe_3O_4/PANI nanocomposites and its corrosion resistance mechanism in waterborne acrylate-amino coating. *Progress in Organic Coating*, **133**, 117–124.

26. Park, C. M., Wang, D., Han, J., Heo, J. and Su, C. (2018) Evaluation of the colloidal stability and adsorption performance of reduced graphene oxide-elemental silver/magnetite nanohybrids for selected toxic heavy metals in aqueous solutions. *Applied Surface Science*, **471**, 8–17.

27. Maham, M., Nasrollahzadeh, M., Sajadi, S. M. and Nekoei, M. (2017) Green synthesis of CuO nanoparticles by aqueous extract of *Gundelia tournefortii* and evaluation of their catalytic activity for the synthesis of *N*-monosubstituted ureas and reduction of 4-nitrophenol. *Journal of Colloid and Interface Science*, **455**, 245–253.

28. Sujiono, E. H., Zurnansyah, Zabrian, D., Dahlan, M. Y., Amin, B. D., Samnur and Agus, J. J. (2020) Graphene oxide based coconut shell waste: synthesis by modified Hummers method and characterization. *Heliyon*, **6**, 4568.

29. Weng, Y. K., Rosli, A. R. M. and Yusoff, F. (2019) Magnetite graphene for electrochemical determination of uric acid. *Malaysian Journal of Analytical Sciences*, **23(3)**, 407.

30. Rosli, A. R., Loh, S. H. and Yusoff, F. (2019) Synthesis and Characterization of Magnetic Fe_3O_4/ Reduced Graphene Oxide and its Application in Determination of Dopamine. *Asian Journal of Chemistry*, **31(12)**, 2785–2792.

31. Muhamad, N. B. and Yusoff, F. (2018) Synthesis and Characterization of Gold Nanoparticles Decorated Poly(3,4-Ethylenedioxythiophene) on Graphene for Prospective Cathode Catalyst in Fuel Cell. *Journal of Sustainability Science and Management*, **13**, 19–27.

32. Chen, L., Batchelor-McAuley, C., Rasche, B., Johnston, C., Hindle, N. and Compton, R. G. (2020) Surface area measurements of graphene and graphene oxide samples: Dopamine adsorption as a complement or alternative to methylene blue? *Applied Materials Today*, **18**, 100506.

33. Muhamad, N. A. B. and Yusoff, F. (2018) The Physical and Electrochemical Characterization of Gold Nanoparticles Supported PEDOT/Graphene Composite as Potential Cathode Material in Fuel Cells. *Malaysian Journal of Analytical Sciences*, **22(6)**, 921–930.

34. Ismail, N. A., Arris, F. A., Tumian, A. and Wan Salim, W. W. A. (2019) Preliminary study on the effect of reduced graphene oxide, gold nanoparticles, and nafion® concentration on redox peak current for electrochemical biosensing. *Journal of Engineering Science and Technology*, **14(1)**, 48–58.

35. Elgrishi, N., Rountree, K. J., McCarthy, B. D., Rountree, E. S., Eisenhart, T. T. and Dempsey, J. L. (2018) A practical beginner's guide to cyclic voltammetry. *Journal of Chemical Education*, **95(2)**, 197–206.

36. Shi, R., Liang, J., Zhao, Z., Liu, A. and Tian, Y. (2017) An electrochemical bisphenol A sensor based on one step electrochemical reduction of cuprous oxide wrapped graphene oxide nanoparticles modified electrode. *Talanta*, **169**, 37–43.

37. Suresh, K. and Yusoff, F. (2020) Thermal stability and porosity of reduced graphene oxide/zinc oxide nanoparticles and their capacity as a potential oxygen reduction electrocatalyst. *Malaysian Journal of Analytical Science*, **24(3)**, 405–412.

38. Chen, X., Chen, J., Dong, H., Yu, Q., Zhang, S. and Chen, H. (2019) Sensitive detection of dopamine using a platinum microelectrode modified by reduced graphene oxide and gold nanoparticles. *Journal of Electroanalytical Chemistry*, **848**, 113244.

39. Muhamad, N. B., Khairul, W. M. and Yusoff, F. (2019) Synthesis and characterization of poly (3,4-ethylenedioxythiophene) functionalized graphene with gold nanoparticles as a potential oxygen reduction electrocatalyst. *Journal of Solid State Chemistry*, **275**, 30–37.

40. Ramachandran, R., Leng, X., Zhao, C., Zu, Z. X. and Wang, F. (2020) 2D siloxene sheets: A novel electrochemical sensor for selective dopamine detection. *Applied Materials Today*, **18**, 100477.

41. Jo, J., Lee, S., Gim, J., Song, J., Kim, S., Mathew, V., Alfaruqi, M. H., Kim, S., Lim, J. and Kim, J. (2019) Facile synthesis of reduced graphene oxide by modified Hummer's method as anode material for Li-, Na-, and K-ion secondary batteries. *Royal Society Open Science*, **6(4)**, 181978–181990.

42. Wondimu, T. H., Chen, G. C., Kabtamu, D. M., Chen, H. Y., Bayeh, A. W., Huang, H. C. and Wang, C. H. (2018) Highly efficient and durable phosphine reduced iron-doped tungsten oxide/ reduced graphene oxide nanocomposites for the hydrogen evolution reaction. *International Journal of Hydrogen Energy*, **43(13)**, 6481–6490.